RSC Advances

Journal Name

ARTICLE

Facile fabrication of reduced graphene oxide covered ZnCo$_2$O$_4$ porous nanowire arrays hierarchical structure on Ni-foam as a high performance anode for lithium-ion battery

Yujue Wang,[a] Yongzhi Zhang,[b] Junke Ou,[c] Qian Zhao,[d] Mei Liao,[a] and Dan Xiao*[ad]

We successfully prepared a nanostructure of ZnCo$_2$O$_4$ nanowire arrays directly grown on Ni-foam substrate with its surface decorated by reduced graphene oxide (rGO) through a very simple and cost-effective two-step facile fabrication of hydrothermal method together with cacination treatment followed by electro-deposition. It is shown that there are plenty of pores distributing each of the nanowire, providing large specific surface area. In the mean time we can also observe that the rGO thin flakes have indeed covered the the ZnCo$_2$O$_4$ nanowires. This binder-free hierarchical composite on Ni substrate was further taken as anode for lithium ion batteries. It displays largely improved electrochemical performance of high capacity, excellent cycling stability and good rate capability than both the one without rGO covering and the one with binder and conductive additive. It can retain a high discharge capacity of 1208 mAh g^{-1} after 100 cycles at the rate of 0.1 A g^{-1}, and in the mean time, it can also provide a high capacity of 1032 mAh g^{-1} after 100 cycles even at a high rate of 0.5 A g^{-1}. In this paper do we prove that our rGO covered ZnCo$_2$O$_4$ nanowire arrays hierarchical structure supported on Ni-foam substrate is a promising anode material for high performance lithium storage devices.

Introduction

Nowadays, rechargeable lithium ion batteries (LIBs) have become the regnant energy source which is widely used in our life and people's urges of energy materials applied in electronic devices and electric vehicles are turning increasingly intense. The most commonly utilized anode material for commercial LIBs, the graphite, could hardly meet people's needs because its theoretical specific capacity is quite low (only 372 mAh g^{-1}), and moreover, the rate capability is relatively poor.[1-3] With this, it is attracting more extensive attentions researching and developing advanced electrode materials of high performance, low price and benignity to environment for LIBs which could be a substitute for the electrode of graphite.[1-8]

As a result, people have widely exploited transition metal oxides as anode materials for LIBs, for instance, TiO$_2$, Fe$_2$O$_3$, Co$_3$O$_4$, SnO$_2$, etc., because they can perform high reversible capacities of about

500~1000 mAh g^{-1} [6, 9-11] and can easily be made on the nanoscale by a solution route.[12] ZnCo$_2$O$_4$ is amongst one of the most promising electrode materials [13-15] for it is of large capacity, less toxicity and lower cost than the widely studied Co$_3$O$_4$.[16, 17] However, its poor conductivity and evident volume change in the process of Li$^+$ intercalation and de-intercalation reaction could give rise to rupture of electrode films in the process of electrical isolation, further resulting in rapid capacity fading. These disadvantages make up a big barrier in the application in LIBs.[18]

Nowadays, graphene and graphene oxide (GO) are the most promising materials,[19] having applications in the field of physics,[20] chemistry [21] and material science.[22] Conductivity of highly reduced monolayer of GO range between 0.05 and 2 S cm^{-1},[23] together with its water solubility, making it promising to construct nanocomposite with other materials via a simple aqueous elctro-deposition way for electrochemical usage with improved performance.[24-26]

Therefore, we prepared rGO covered ZnCo$_2$O$_4$ nanowire arrays nanostructure directly on Ni-foam using a simple two-step fabrication of hydrothermal method together with annealing treatment followed by electro-deposition. It possesses several advantages: (1) both the two steps of hydrothermal method and electro-deposition are of low cost, easy operation and effectivity; (2) not only could the rGO shell improve conductivity, but it could also cover the ZnCo$_2$O$_4$ arrays and prevent it from peeling off and crushing, thus enhance the rate capability and retard the capacity fading; (3) this 3D hierarchical structures can utilize not only their unique size and shape for electrons and Li$^+$ to transport in solid state, but their large surface area for increased active material-

a. *College of Chemistry, Sichuan University, 29 Wangjiang Road, Chengdu 610064, China. E-mail: xiaodan@scu.edu.cn; Fax: +86-28-85412907; Tel: +86-28-85416218*
b. *Institute of New Energy and Low-Carbon Technology, Sichuan University, No.24 South Section 1, Yihuan Road, Chengdu 610065, China. Fax: +86-28-6213-8325; Tel: +86-28-6213-8375*
c. *School of Basic Medical Sciences & Nursing, Chengdu University, Shiling Town, Chengdu 610106, China. E-mail: ojk0001@163.com*
d. *College of Chemical Engineering, Sichuan University, 29 Wangjiang Road, Chengdu 610064, China. E-mail: xiaodan@scu.edu.cn; Fax: +86-28-85415029; Tel: +86-28-85416029*
† Electronic Supplementary Information (ESI) available. See DOI: 10.1039/x0xx00000x

electrolyte contact.[27-31] (4) moreover, the absence of binder and conductive additive could increase electrolyte accessibility to active material, so that we can achieve higher performance as an anode material for LIBs.[32] With these unique merits of our 3D hierarchical structure of rGO covered $ZnCo_2O_4$ nanowire arrays, it displays improved rate capability and cycling stability.

Experimental

Materials preparation

Pre-treatment. Ni-foam substrate (3 cm × 4 cm) was first treated under ultrasound in acetone and ethanol for 20 min respectively to wipe off possible oil stain on the surface. Then the substrate was immersed into 0.5 M hydrochloric acid (HCl) solution under ultrasound for 10 min in order to get rid of the probable oxide layer before it was washed by distilled water and ethanol and dried in vacuum oven overnight.

Synthesis of $ZnCo_2O_4$ nanowire arrays (ZNW) on Ni-foam (ZNW-Ni). The chemicals in the experiment are all analytical grade and directly used. In a typical synthesis process, 1 mmol zinc nitrate ($Zn(NO_3)_2 \cdot 6H_2O$) and 2 mmol cobalt nitrate ($Co(NO_3)_2 \cdot 6H_2O$) were dissolved in 70 mL distilled water to give a clear pink solution, after which added 5 mmol urea ($CO(NH_2)_2$) and 2 mmol ammonium fluoride (NH_4F) gradually at room temperature. After intense stirring for several minutes till it turned homogeneous, the solution was transferred into a Teflon-lined stainless-steel autoclave, reacted at 120 °C for 5 h and cooled to room temperature naturally. The samples were washed with distilled water and ethanol for several times and dried at 60 °C overnight. Finally, the samples were placed in a tube furnace and annealed at 400 °C for 2 h.

Synthesis of rGO covered $ZnCo_2O_4$ nanowire arrays (ZNWG) on Ni-foam (ZNWG-Ni). The reduced grapheme oxide (rGO) was covered on the as prepared ZNW on Ni-foam by electrochemical deposition, with the ZCO-grown Ni-foam (1 cm × 1 cm) working as the working electrode, saturated calomel electrode as the reference electrode and Pt plate as the counter electrode in an aqueous electrolyte solution of graphene oxide (GO) and 0.1 M disodium hydrogen phosphate (Na_2HPO_4), in a potential range of -2~0 V at a constant current of 2 mA at room temperature. GO was synthesized from graphite powder through a modified Hummers' method.[33-35]

Material characterization

Several different techniques were applied to characterize the samples we have prepared. The crystal structure of the samples were characterized using an X-ray diffractometer (XRD; Tongda TD-3500, Liaoning, China) with Cu Kα radiation (λ = 1.5418 Å) running at 30.0 kV and 20.0 mA. Scanning electron microscopy (SEM) was operated on a Hitachi S4800 scanning electron microscope (Tokyo, Japan) to analyze the morphology of samples. Transmission electron microscopy (TEM) and high-resolution transmission electron microscopy (HRTEM) were performed on a FEI Tecnai G2 20 TEM (Hillsboro, OR, USA) operating at 200 kV. Inductively coupled plasma atomic emission spectroscopy (ICP-AES) was performed using an IRIS Advantage (ThermoElemental, USA). Carbon content was determined on a EuroEA3000 Analyzer (Leeman, USA). The specific surface area and pore size distribution were obtained from the results of nitrogen (N_2) adsorption and desorption on an automated gas sorption system (Quantachrome NOVA 1000e apparatus) using Brunauer-Emmett-Teller (BET) and Barrett-Joyner-Halenda (BJH) technique. Raman measurements were carried out on a LabRAM HR800 spectrometer (HORIBA Jobin Yvon, France). Thermogravimetric analysis (TGA) was conducted on a Henven HCT-2 thermal analyzer (Beijing, China). X-ray photoelectron spectroscopy (XPS) characterization was operated on a Kratos XSAM800 spectrometer (Manchester, UK), with a MgKα X-ray (1253.6 eV) excitation source running at 15 kV, a hemispherical electron energy analyzer and a multichannel detector.

Electrochemical measurements

The Ni-foam covered with $ZnCo_2O_4$ was cut into many small pieces. The loading density of the as-prepared samples were around 1.05 to 1.76 mg cm^{-2}, and each piece of the samples were used directly as working electrode without any addition of both acetylene black and binder. In comparison, we also collected the ZNW powder (ZP) scraped from the Ni-foam and formed it into working electrodes. The electrodes were prepared with the mixing of 80 wt% active material, 10 wt% polyvinylidene fluoride (PVDF) and 10 wt% acetylene black (AB) before dispersing into N-methylpyrrolidone (NMP) to form a uniform slurry. Then the slurry was spread on copper foil evenly and vacuum dried at 100 °C. Samples were assembled into CR2032 coin-type cells in a glovebox (Delix LS800S, Sichuan, China) filled with Ar, using the ZNWG, ZNW on Ni-foam (ZNWG-Ni and ZNW-Ni) and ZP as anode materials, Li-metal foil as both counter and reference electrode, a piece of Celgard 2300 microporous film as separator, and $LiPF_6$ solution of 1.0 M in ethylene carbonate (EC) and dimethyl carbonate (DMC) (volumetric ratio EC:DMC=1:1) as the electrolyte. Before the measurement aged the cell for 24 h in order to make sure that the electrolyte was fully permeated into the electrodes.

Then the electrochemical measurements were carried out and the coin-type half cells were cycled at a voltage range of 0.01~3 V (vs. Li$^+$/Li) and different current densities using a multichannel battery measurement system (Land, Hubei, China) at room temperature. The electrochemical impedance spectroscopy (EIS) and cyclic voltammetry (CV) were performed on an electrochemical workstation (Autolab PGSTAT 30/302, Eco Chemie B.V., Amsterdam, the Netherlands). The voltage range and scan rate of the CV measurement was 0.01~3 V and 0.1 mV s^{-1}, respectively.

Results and discussion

The morphology of the as-prepared $ZnCo_2O_4$ nanowire arrays (ZNW) and rGO covered $ZnCo_2O_4$ nanowire arrays (ZNWG) on Ni-foam are shown in Fig. 1 and 2 using scanning electron microscopy (SEM, Fig. 1) and transmission electron microscopy (TEM, Fig. 2), respectively. Fig. 1a and b show the low magnification SEM of ZNW-Ni and ZNWG-Ni, respectively, with the contrast revealing that the $ZnCo_2O_4$
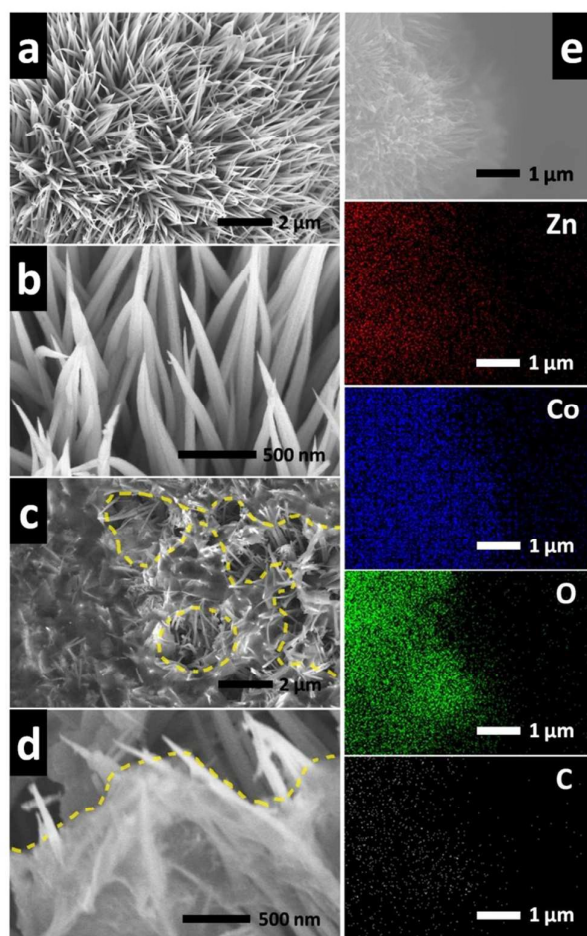
Fig. 1 (a-d) SEM images of ZNW (a and b) and ZNWG (c and d) grown on Ni-foam, respectively. The yellow dash lines marked in (c) and (d) represent the boundary of rGO covered and none rGO covered areas. (e) SEM image of a bunch of ZNWG and the corresponding SEM-EDS elemental mapping of Zn, Co, O and C.

nanowires of ZNWG-Ni were covered by transparent thin films. The zoom-in SEM images are shown in Fig. 1b and d, which give a clearer view of the 3D nanostructure of the as-prepared nanowires and the presence of rGO film. It is shown obviously that the diameter of the nanowires was about 100 nm and we can also observe plentiful pores distributing the whole trunk. In low magnification SEM of ZNWG-Ni (Fig. 1c), we can see some dim areas likely to be covered by a layer of thin film, evidently distinct from that of ZNW-Ni, emphasized by yellow dash lines showing the boundary of covered and none-covered areas. We could have a clearer view in the zoom-in image (Fig. 1d) which displays obviously a transparent film, indicating that the $ZnCo_2O_4$ nanowires were covered with rGO film. For further confirmation that the rGO film really connectively decorated to the whole surface of ZNW, TEM investigation was carried out for both ZNW (Fig. 2a and b) and ZNWG (Fig. 2c and d). In contrast, we can see that on the surface of $ZnCo_2O_4$ nanowires before electro-deposition appeared no film (Fig.

2a and b), while on that of $ZnCo_2O_4$ nanowires after electro-deposition exhibited a layer of thin film (Fig. 2c and d), which further verified the rGO was indeed decorated to the surface of ZNW. With these, the fabrication process of ZNWG on Ni-foam is concluded and shown as a schematic illustration in Fig. 3.

To determine the crystal structure of both the ZNW and ZNWG, X-ray Diffraction (XRD) was carried out, with patterns shown in Fig. 2e. Three strong diffraction peaks ascribed to the Ni-foam substrate were found in the pattern, which is marked with symbol ◇, while another seven diffraction peaks marked with symbol ∇ which correspond to that of cubic $ZnCo_2O_4$ with spinel structure (JCPDF card 23-1390) were also displayed in the pattern. Additionally, no obvious extra diffraction peaks were detected, indicating that the product is of high purity.

ICP-AES analysis was conducted to obtain the metal ion contents in the as-prepared ZNWG, further confirm its pure phase. The result shows that the contents of Zn and Co are 12.9 and 22.3 ppm, respectively, 1:1.92 in molar ratio, which agree well with the molar ratio of Zn and Co of 1:2 in $ZnCo_2O_4$, further confirming its pure phase.

Raman measurement was proceeded in order to further confirm the existence of rGO. Fig .4 shows the Raman spectra for ZNWG and GO. The bands within the ranges of 250-700 and 880-1200 cm^{-1} belong to $ZnCo_2O_4$, while the ones in ranges of 1200-1450 and 1500-1650 cm^{-1} are ascribed to the D band (K-point phonons of A1g symmetry) and G-band (E2g phonons of the C sp2 atoms) of GO,
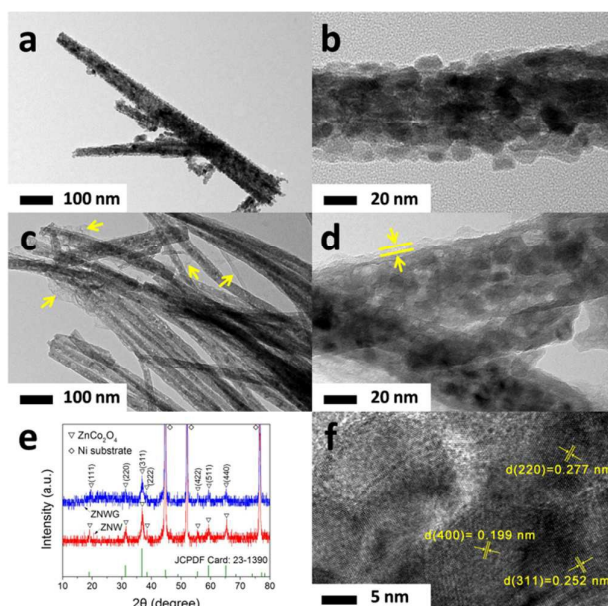

Fig. 2 (a-d) Typical TEM images of branches of ZNW (a, b) and ZNWG (c, d), with the yellow arrows pointing out the presence of rGO thin film. (e) XRD patterns of as-prepared ZNW (red) and ZNWG (blue) on Ni-foam, with symbol "∇" and "◇" representing the diffraction peaks of $ZnCo_2O_4$ and Ni, respectively. (f) HRTEM image of a ZNWG branch.
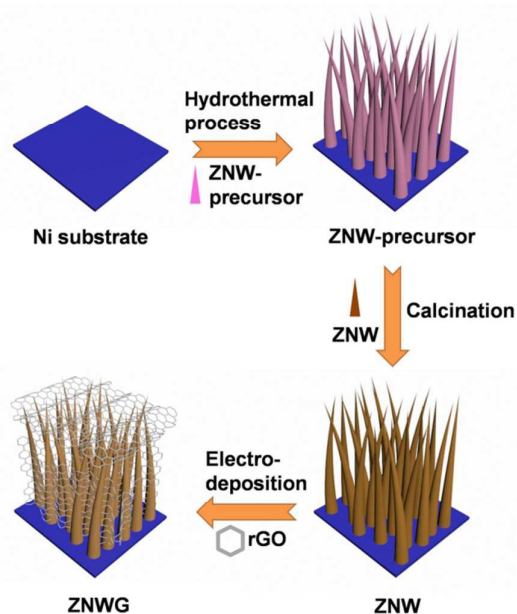
Fig. 3 Schematics of the fabrication process of ZNWG on Ni-foam substrate.

respectively, demonstrating the presence of GO in the composite. Compared to GO, the G band of GO in ZNWG shifts to low frequency, indicating a significant removal of oxygen-containing groups on GO during electro-deposition.[36] That's why we call it rGO. It is easily observed that ZNWG shows a lower intensity of D and G band ($I_D/I_G = 0.90$) than GO freeze-dried from the GO dispersion ($I_D/I_G = 0.99$), which illustrate the electronic conjugation after reduction, leading to high electronic conductivity.[37]

In order to obtain the load of rGO in ZNWG, thermogravimetric analysis (TGA) measurement was operated for ZNWG and ZNW samples in air atmosphere to acquire carbon content (Fig. S1). The little weight loss below in the very beginning could be ascribed to the moisture in the samples. By comparing the two curves, it is easy to find that the content of rGO is 1.39%, which agrees with the result of C, H, N, S test of 1.28%.
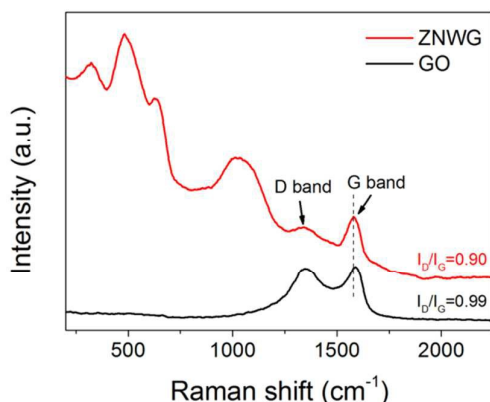

Fig. 4 Raman spectra of ZNWG (red) and pure GO (black).
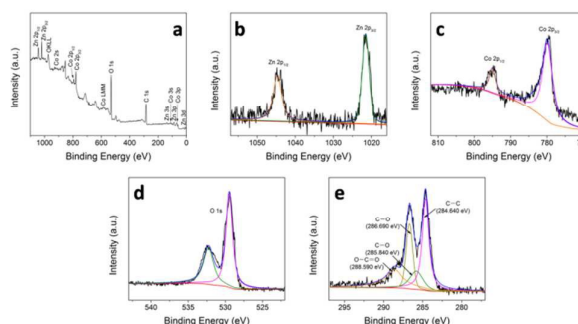
Fig. 5 XPS spectra of ZNWG: (a) survey spectrum and high resolution (b) Zn 2p, (c) Co 2p, (d) O 1s, (e) C 1s spectra.

Chemical states of the as-prepared ZNWG sample were studied via X-ray photoelectron spectroscopy (XPS) in order to further confirm the purity of the sample, the appearance of rGO and the combination form between rGO and $ZnCo_2O_4$ nanowires. Fig. 5a shows a full wide-scan spectrum of ZNWG. Characteristic peaks for Zn, Co, O, and C elements are easily observed. The binding energy in XPS analysis for C 1s peak at 284.6 eV was used as the reference for calibration. Fig. 5b shows the high-resolution Zn 2p spectrum. Two peaks with binding energy values of 1021.480 and 1044.735 eV are ascribed to Zn $2p_{3/2}$ and Zn $2p_{1/2}$, indicating the Zn(II) oxidation state of $ZnCo_2O_4$.[38, 39] Fig. 5c shows the high-resolution Co 2p spectrum. Two strong peaks at 779.991 eV and 790.063 eV for Co $2p_{3/2}$ and Co $2p_{1/2}$ are observed, respectively, confirming the Co(III) oxidation state of $ZnCo_2O_4$.[38, 40] The O 1s peaks at 529.480 and 532.243 eV correspond to the oxygen species in $ZnCo_2O_4$, shown in Fig. 5d.[15] From these, the XPS results in conjunction with XRD data confirm the formation of $ZnCo_2O_4$ with normal spinel structure. The C 1s spectrum in Fig. 5e possesses four main peaks that correspond to functional groups of carbonyl carbon in acetone/quinone, carboxylic carbon in –COOR (R=H and alkyl), ether/phenolic carbon in C–O–C and C–OH, and carbon atoms in the graphene planes.[41] Comparing with the XPS spectra of ZNW shown in Fig S2, no evident distinction is found in the corresponding high resolution Zn 2p, Co 2p and O 1s spectra, and no other forms of C is observed in the C 1s spectrum except for the ones mentioned above. These are all similar to previous works of metal oxide with rGO or graphene physically coated.[42, 43] Furthermore, from the XRD patterns of ZNWG and ZNW in Fig. 2e, we can see that there is no obvious distinction between the two samples. No other peaks except for those of $ZnCo_2O_4$ have been observed. So it can be confirmed that rGO is not chemically bound but physically coated to the $ZnCo_2O_4$ nanowires during electrochemical deposition process.

By reason of the plentiful pores observed in SEM and TEM images, BET measurement of N_2 adsorption and desorption was carried out to determine the specific surface area of the as-prepared ZNWG and ZNW, shown in Fig. 6. The as-prepared ZNWG sample displays a specific surface area of 76.32 m^2 g^{-1}, larger than that of ZNW of
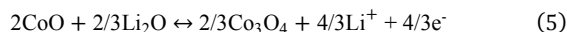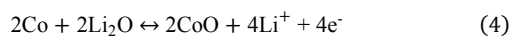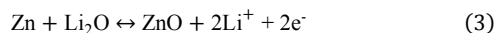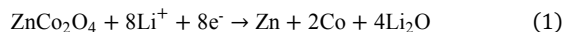
ARTICLE
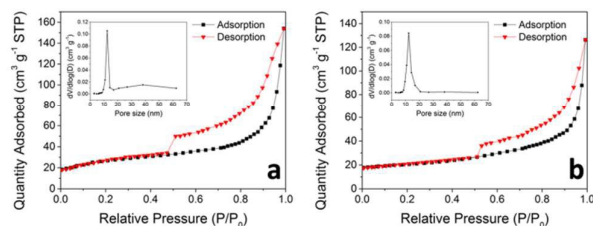
Fig. 6 Nitrogen adsorption and desorption isotherms and corresponding pore size distribution (inset) deduced from desorption data and computed from the isotherm employing BJH model of ZNWG scrapped from Ni-foam substrate.

68.13 $m^2\ g^{-1}$. The appearance of rGO has increased the specific area to a certain degree, and the extent of electrolyte-material contact could be improved due to the large specific surface area, bringing about sufficient electrochemical reaction.[44]

The pore size distribution deduced from desorption data and computed from the isotherm employing BJH model (inset of Fig. 6a and b) show that most of the pores in the nanowires are within the size range of 10 to 20 nm for both ZNWG and ZNW. This porous nanostructure can buffer the large volume change of the electrode during the repeated Li^+ intercalation and de-intercalation.[44]

Typical electrochemical procedure of $ZnCo_2O_4$ concerned lithium intercalation and de-intercalation reactions, as reported in previous literatures, is shown as follows:[14, 18]

$$ZnCo_2O_4 + 8Li^+ + 8e^- \rightarrow Zn + 2Co + 4Li_2O \quad (1)$$

$$Zn + Li^+ + e^- \rightarrow LiZn \quad (2)$$

$$Zn + Li_2O \leftrightarrow ZnO + 2Li^+ + 2e^- \quad (3)$$

$$2Co + 2Li_2O \leftrightarrow 2CoO + 4Li^+ + 4e^- \quad (4)$$

$$2CoO + 2/3Li_2O \leftrightarrow 2/3Co_3O_4 + 4/3Li^+ + 4/3e^- \quad (5)$$

Electrochemical measurements of cyclic voltammetry (CV) and galvanostatic discharging and charging have been conducted to test the electrochemical performance of as-prepared ZNWG-Ni electrode. CV measurement was carried out at a scan rate of 0.1 mV s^{-1} and in a voltage range of 0.01-3 V. First three CV curves of ZNWG-Ni electrode are shown in Fig. 7g. In the first cathodic process, it shows up an obvious sharp irreversible reduction peak at approximately 0.62 V, which is correlated to the solid electrolyte interface (SEI) layer formation and the irreversible reduction of $ZnCo_2O_4$ to Zn and Co shown in reaction 1.[18, 45] Then in the first anodic scanning process could we observe two broad peaks at about 1.65 and 2.25 V, on account of the oxidation of Zn and Co to Zn^{2+} and Co^{2+}, respectively, displayed in reaction (3-5). From the 2nd cycle on, the reduction peak moves to a higher potential of approximately 0.9 V and transforms into a broader one, which differs from the 1st cycle, indicating that the two processes involve in different electrochemical reactions. The similar shape of the CV
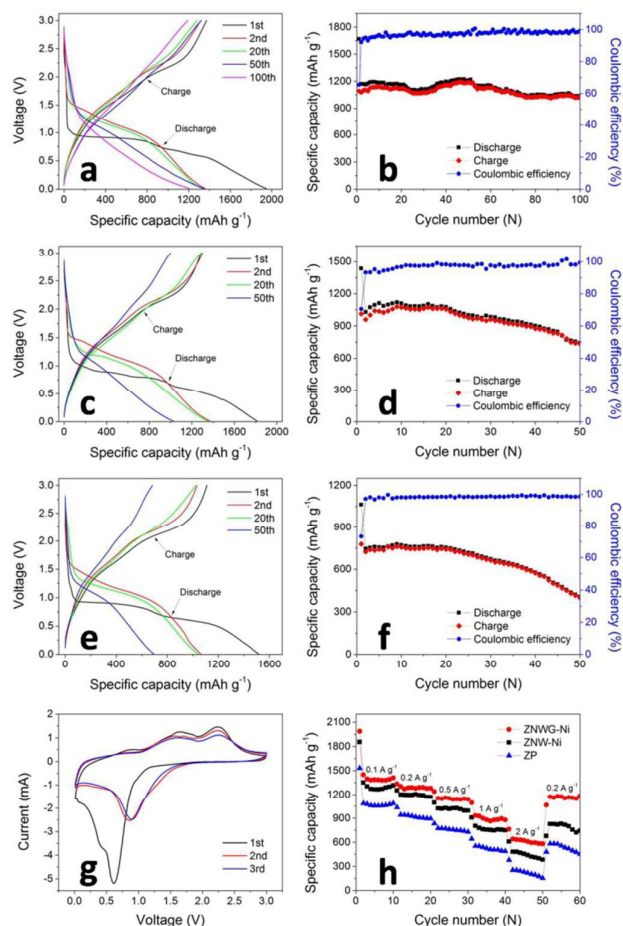
Fig. 7 (a, c and e) Galvanostatic discharge and charge profile of ZNWG-Ni (a), ZNW-Ni (c) and ZP (e) electrode at a current density of 0.1 A g^{-1}; (b, d and f) cycling performance of ZNWG-Ni (b), ZNW-Ni (d) and ZP (f) electrode at a current density of 0.5 A g^{-1} with corresponding Coulombic efficiencies; (g) first three CV curves of ZNWG-Ni electrode at a scan rate of 0.1 mV s^{-1}; (h) rate capabilities of ZNWG-Ni, ZNW-Ni and ZP electrode at different current densities. Corresponding active material loadings of the electrodes above are shown in Table S1.

curves of the 2nd and 3rd cycle indicates good reversibility of the electrode from the 2nd cycle on.

Fig. 7a, c and e show the discharge and charge curves for the first 100 cycles at a current density of 0.1 A g^{-1} in a voltage range of 0.01-3 V. In the first discharge procedure, the voltage suddenly dropped to approximately 1 V, which was due to the conversion reaction as shown in reaction 1, and it is in accordance with CV result. Then there exists a long plateau at about 1 V, followed by a slope beneath 1 V, and this has been fully discussed in previous papers.[15, 18, 45] From the 2nd cycle on, the long discharging plateau changed into a slope, which agreed well with some previous reports,[18, 46] indicating that a stable solid electrolyte interface (SEI) has formed during the first cycle.[47] The initial discharge and charge
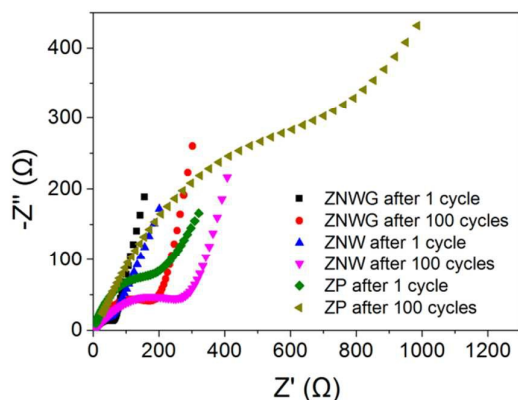
Fig. 8 Nyquist plots of ZNWG, ZNW and ZP electrode for the 1st and 100th cycle, respectively.

capacities for ZNWG-Ni electrode were 1946 and 1371 mAh g^{-1}, respectively, as shown in Fig. 7a. The high initial discharge capacity might be on account of its large surface area. Due to the formation of SEI and Li$_2$O during the reduction of metal oxide to metal,[48-50] the irreversible capacity of the first cycle lost 29.5%. The discharge and charge capacity and relative Coulombic efficiency of ZNWG-Ni over 100 cycles under 0.5 A g^{-1} is shown in Fig. 7b. It can be seen that a very high reversible discharge capacities of 1170 mAh g^{-1} was attained, and even after 100 cycles, it still retained 1032 mAh g^{-1}, which indicated an excellent cycling performance of the ZNWG-Ni electrode. The increase of capacity from the 20th to 50th cycle was most likely to be the result of material activation due to the fully contact with electrolyte and the reversible growth of polymeric gel-like film on account of kinetically activated electrolyte degradation.[51, 52] Additionally, in the 2nd cycle, the Coulombic efficiency rose from 65.5% of the 1st cycle to 94%, and kept over 96% after the 10th cycle, indicating a good reversibility of the ZNWG-Ni electrode.

For comparison, the electrochemical performances of ZNW-Ni and ZP electrode were also tested. Fig. 7c and e show the voltage versus capacity profile of ZNW-Ni and ZP at 0.1 A g^{-1}, respectively. The initial discharge and charge capacities for ZNW-Ni electrode were 1814 and 1287 mAh g^{-1} respectively, besides, 1515 and 1110 mAh g^{-1} for ZP electrode. For ZNW-Ni electrode at 0.5 A g^{-1}, at the beginning, its reversible discharge capacity of 1094 mAh g^{-1} was just a little lower than that of ZNWG-Ni electrode. However, from the 20th cycle on, the capacity began to fall, and only after 50 cycles, it dropped to 742 mAh g^{-1}, merely retained 67.8% of its initial capacity, as shown in Fig. 7d. Much worse for ZP electrode as shown in Fig. 7f, its initial reversible discharge capacity was only 745 mAh g^{-1}, and what's more, the capacity began to drop from the 20th cycle, with only 405 mAh g^{-1} (54.4% of the initial reversible capacity) retained after 50 cycles. These comparison measurements demonstrated that the performance of ZNWG-Ni electrode is much higher than both ZNW-Ni and pasted electrode of ZP.

Further demonstration of the remarkable performance of ZNWG-Ni electrode was conducted by studying the electrochemical property of rate capability from a current density of 0.1 A g^{-1} to 1 A g^{-1}, as shown in Fig. 7h. With the current density varying following a 0.1, 0.2, 0.5, 1 to 2 A g^{-1} increase, the corresponding discharge capacity followed a decrease of 1396, 1288, 1153, 932 to 640 mAh g^{-1}, respectively. Even at a high rate of 2 A g^{-1}, it could still provide a reversible capacity of 640 mAh g^{-1}, much higher than that of the 372 mAh g^{-1} of graphite. Moreover, the discharge capacity could restore to 1171 mAh g^{-1} and maintained when the current density changed back to 0.2 A g^{-1} after the high rate cycles above. However, for ZNW-Ni electrode, when current density increased following the same variation above, capacity decreased from 1303, 1201, 1021, 803 to 481 mAh g^{-1}, and with only 826 mAh g^{-1} left when current density changed back to 0.2 A g^{-1}. Things went worse for ZP electrode, with a decrease from 1085, 941, 774, 553 to 253 mAh g^{-1} following the same variation, and only 582 mAh g^{-1} remained at 0.2 A g^{-1} again, inferior to ZNWG-Ni electrode. Additionally, even comparing to other works reported previously, our ZNWG electrode can still keep ahead (Table S2).

The high capacity of ZNWG-Ni electrode could be due to its 3D porous nanowire structure and the direct growth on Ni-foam substrate. The pores in the nanowire structure notably increased the material-electrolyte contacting area and had access to more Li-ion discharge/charge sites,[48, 53-55] meanwhile the direct growth could made it better contact to current collector, thus shortened the charge transfer pathway and lowered the Li$^+$ exchange resistance between active material and electrolyte.[4, 54, 55] These both achieved an efficient electron conduction and collection to current collector, accommodated the stress arose from the volume change during the Li$^+$ intercalation and de-intercalation process with more void space. It is worth mentioning that the capacity of rGO is only 33 mAh g^{-1} at the rate of 0.5 A g^{-1}, shown in Fig. S3. Together with the similar capacities of ZNW-Ni and ZNWG-Ni electrode, we could say that rGO contributed little to capacities. Moreover, rGO played a big role in improving cyclability and rate capability, as the comparison in Fig. 7 shows. The superior cycling stability and fine rate capability were not only on account of the large material-electrolyte contacting area and full contact with conducting substrate, but ascribed to the presence of rGO covering the surface of ZnCo$_2$O$_4$ nanowires. It could be inferred that rGO prevented the ZnCo$_2$O$_4$ nanowires from collapse and falling out from Ni-foam by wrapping the nanowires and covering them tightly to the substrate, as Fig. 3 shows, yet for the none rGO covered electrodes, for instance both ZNW-Ni and ZP, the structure would fall down and peeled off from the substrate after several cycles, leading to quick capacity fades. In order to prove this inference, SEM measurement was carried out again to obtain images of both ZNW and ZNWG on Ni-foam after 50 cycles at a current density of 0.5 A g^{-1}, shown in Fig. S4. It is obvious that the shape of ZNW changed and the structure evidently collapsed after 50 cycles, while those of ZNWG show little change, only with a bit of fracture of the nanowires.

Further characterizations of electrochemical impedance spectroscopy (EIS) for the ZNWG-Ni, ZNW-Ni and ZP electrodes were carried out. The Nyquist plots of the three electrodes after the first cycle were shown in Fig. 8, which displays a semicircle and a straight line in the high and low frequency region, respectively. Relevant solution resistance (R_s) and calculated charge transfer resistance (R_{ct}) of the cells are shown in Table S3. It is obvious that the charge transfer resistance of ZNWG electrode in the initial and after 100 cycles are smaller than the corresponding ones of both ZNW and ZP electrode. In the mean time, the increase in R_{ct} after long cycling is also smaller than that of both ZNW and ZP electrode. Therefore, the ZNWG electrode can maintain its integrity better, leading to longer cycle life.

Conclusions

In summary, we prepared a hierarchical $ZnCo_2O_4$ nanowire structure covered by rGO directly on Ni-foam substrate for lithium ion batteries with no binder and conductive agent through a two-step facile fabrication of hydrothermal method together with calcination followed by electrochemical deposition. Comparing with the bare $ZnCo_2O_4$ nanowires grown on Ni-foam and $ZnCo_2O_4$ powder with binder and conductive additive, and even many reported ones, it displayed high specific capacity, excellent cycling stability and fine rate capability. A high capacity of 1170 mAh g^{-1} was reached and retained 1032 mAh g^{-1} even after 100 cycles at 0.3 A g^{-1}. After series of high rate test and returned to low rate of 0.2 A g^{-1}, it could still maintain a reversible capacity of 1171 mAh g^{-1}. These good electrochemical performance of our electrode could be on account of not only the full material-electrolyte contact and available areas for Li^+ intercalation and de-intercalation, the accommodation of the stress arose from the volume change and the efficient electron conduction and collection to current collector provided by the hierarchical and porous structure, but also ascribed to the presence of rGO that prevented the nanowires from collapse and falling out from Ni-foam by wrapping the nanowires and covering them tightly to the substrate. It will be a promising anode material for high performance lithium ion batteries.

Acknowledgements

Notes and references

1. K. Kang, Y. S. Meng, J. Bréger, C. P. Grey and G. Ceder, *Science*, 2006, 311, 977-980.
2. B. Scrosati, *Nat. Nanotechnol.*, 2007, 2, 598-599.
3. M. Armand and J.-M. Tarascon, *Nature*, 2008, 451, 652-657.
4. K. T. Nam, D. W. Kim, P. J. Yoo, C. Y. Chiang, N. Meethong, P. T. Hammond, Y. M. Chiang and A. M. Belcher, *Science*, 2006, 312, 885-888.
5. J. M. Tarascon and M. Armand, *Nature*, 2001, 414, 359-367.
6. P. Poizot, S. Laruelle, S. Grugeon, L. Dupont and J. Tarascon, *Nature*, 2000, 407, 496-499.
7. A. S. Arico, P. Bruce, B. Scrosati, J. M. Tarascon and W. Van Schalkwijk, *Nat. Mat.*, 2005, 4, 366-377.
8. B. Kang and G. Ceder, *Nature*, 2009, 458, 190-193.
9. D. V. Bavykin, J. M. Friedrich and F. C. Walsh, *Adv. Mater.*, 2006, 18, 2807-2824.
10. P. L. Taberna, S. Mitra, P. Poizot, P. Simon and J. M. Tarascon, *Nat. Mat.*, 2006, 5, 567-573.
11. N. Kang, J. H. Park, J. Choi, J. Jin, J. Chun, I. G. Jung, J. Jeong, J. G. Park, S. M. Lee and H. J. Kim, *Angew. Chem.*, 2012, 124, 6730-6734.
12. G. R. Patzke, Y. Zhou, R. Kontic and F. Conrad, *Angew. Chem. Int. Ed.*, 2011, 50, 826-859.
13. R. Alcántara, M. Jaraba, P. Lavela and J. Tirado, *Chem. Mater.*, 2002, 14, 2847-2848.
14. B. Liu, J. Zhang, X. Wang, G. Chen, D. Chen, C. Zhou and G. Shen, *Nano Lett.*, 2012, 12, 3005-3011.
15. L. Hu, B. Qu, C. Li, Y. Chen, L. Mei, D. Lei, L. Chen, Q. Li and T. Wang, *J. Mater. Chem. A*, 2013, 1, 5596-5602.
16. P. Meduri, E. Clark, J. H. Kim, E. Dayalan, G. U. Sumanasekera and M. K. Sunkara, *Nano Lett.*, 2012, 12, 1784-1788.
17. S. Xiong, J. S. Chen, X. W. Lou and H. C. Zeng, *Adv. Funct. Mater.*, 2012, 22, 861-871.
18. Y. Sharma, N. Sharma, G. Subba Rao and B. Chowdari, *Adv. Funct. Mater.*, 2007, 17, 2855-2861.
19. A. K. Geim and K. S. Novoselov, *Nat. Mat.*, 2007, 6, 183-191.
20. K. S. Novoselov, A. K. Geim, S. Morozov, D. Jiang, Y. Zhang, S. a. Dubonos, I. Grigorieva and A. Firsov, *Science*, 2004, 306, 666-669.
21. F. Schedin, A. Geim, S. Morozov, E. Hill, P. Blake, M. Katsnelson and K. Novoselov, *Nat. Mat.*, 2007, 6, 652-655.
22. H. A. Becerril, J. Mao, Z. Liu, R. M. Stoltenberg, Z. Bao and Y. Chen, *ACS nano*, 2008, 2, 463-470.
23. C. Gómez-Navarro, R. T. Weitz, A. M. Bittner, M. Scolari, A. Mews, M. Burghard and K. Kern, *Nano Lett.*, 2007, 7, 3499-3503.
24. L. Chen, Y. Tang, K. Wang, C. Liu and S. Luo, *Electrochem. Commun.*, 2011, 13, 133-137.
25. M. Hilder, B. Winther-Jensen, D. Li, M. Forsyth and D. R. MacFarlane, *Phys. Chem. Chem. Phys.*, 2011, 13, 9187-9193.
26. C. Liu, K. Wang, S. Luo, Y. Tang and L. Chen, *Small*, 2011, 7, 1203-1206.
27. Y. Yu, L. Gu, C. Zhu, S. Tsukimoto, P. A. van Aken and J. Maier, *Adv. Mater.*, 2010, 22, 2247-2250.
28. W. Zhou, C. Cheng, J. Liu, Y. Y. Tay, J. Jiang, X. Jia, J. Zhang, H. Gong, H. H. Hng and T. Yu, *Adv. Funct. Mater.*, 2011, 21, 2439-2445.
29. A. Pan, H. B. Wu, L. Yu, T. Zhu and X. W. Lou, *ACS Appl. Mater. Inter.*, 2012, 4, 3874-3879.
30. L. Li, Y. Cheah, Y. Ko, P. Teh, G. Wee, C. Wong, S. Peng and M. Srinivasan, *J. Mater. Chem. A*, 2013, 1, 10935-10941.

31. X. Li, A. Dhanabalan, L. Gu and C. Wang, *Adv. Energy Mater.*, 2012, 2, 238-244.
32. J. Jiang, Y. Li, J. Liu and X. Huang, *Nanoscale*, 2011, 3, 45-58.
33. W. S. Hummers Jr and R. E. Offeman, *J. Am. Chem. Soc.*, 1958, 80, 1339-1339.
34. N. I. Kovtyukhova, P. J. Ollivier, B. R. Martin, T. E. Mallouk, S. A. Chizhik, E. V. Buzaneva and A. D. Gorchinskiy, *Chem. Mater.*, 1999, 11, 771-778.
35. D. C. Marcano, D. V. Kosynkin, J. M. Berlin, A. Sinitskii, Z. Sun, A. Slesarev, L. B. Alemany, W. Lu and J. M. Tour, *ACS nano*, 2010, 4, 4806-4814.
36. K. N. Kudin, B. Ozbas, H. C. Schniepp, R. K. Prud'Homme, I. A. Aksay and R. Car, *Nano Lett.*, 2008, 8, 36-41.
37. D. V. Kosynkin, A. L. Higginbotham, A. Sinitskii, J. R. Lomeda, A. Dimiev, B. K. Price and J. M. Tour, *Nature*, 2009, 458, 872-876.
38. S. Vijayanand, P. A. Joy, H. S. Potdar, D. Patil and P. Patil, *Sens. Actuat. B*, 2011, 152, 121-129.
39. I. Grohmann, B. Peplinski and W. Unger, *Surf. Interface Anal.*, 1992, 19, 591-594.
40. B. Varghese, C. Teo, Y. Zhu, M. V. Reddy, B. V. Chowdari, A. T. S. Wee, V. Tan, C. T. Lim and C. H. Sow, *Adv. Funct. Mater.*, 2007, 17, 1932-1939.
41. U. Zielke, K. Hüttinger and W. Hoffman, *Carbon*, 1996, 34, 983-998.
42. C. Yuan, L. Yang, L. Hou, J. Li, Y. Sun, X. Zhang, L. Shen, X. Lu, S. Xiong and X. W. D. Lou, *Adv. Funct. Mater.*, 2012, 22, 2560-2566.
43. B. Li, H. Cao, J. Shao, G. Li, M. Qu and G. Yin, *Inorg. Chem.*, 2011, 50, 1628-1632.
44. C. Kim, M. Noh, M. Choi, J. Cho and B. Park, *Chem. Mater.*, 2005, 17, 3297-3301.
45. W. Luo, X. Hu, Y. Sun and Y. Huang, *J. Mater. Chem.*, 2012, 22, 8916-8921.
46. N. Du, Y. Xu, H. Zhang, J. Yu, C. Zhai and D. Yang, *Inorg. Chem.*, 2011, 50, 3320-3324.
47. D. Deng and J. Y. Lee, *Nanotechnology*, 2011, 22, 355401.
48. J. Liu, J. Jiang, C. Cheng, H. Li, J. Zhang, H. Gong and H. J. Fan, *Adv. Mater.*, 2011, 23, 2076-2081.
49. B. Liu, X. Wang, B. Liu, Q. Wang, D. Tan, W. Song, X. Hou, D. Chen and G. Shen, *Nano Res.*, 2013, 6, 525.
50. P. Balaya, H. Li, L. Kienle and J. Maier, *Adv. Funct. Mater.*, 2003, 13, 621-625.
51. X. Wang, X. Li, X. Sun, F. Li, Q. Liu, Q. Wang and D. He, *J. Mater. Chem.*, 2011, 21, 3571-3573.
52. G. Zhou, D. W. Wang, F. Li, L. Zhang, N. Li, Z. S. Wu, L. Wen, G. Q. Lu and H. M. Cheng, *Chem. Mater.*, 2010, 22, 5306-5313.
53. Y. Wang, H. J. Zhang, L. Lu, L. P. Stubbs, C. C. Wong and J. Lin, *ACS Nano*, 2010, 4, 4753-4761.
54. G. Q. Zhang, H. B. Wu, H. E. Hoster, M. B. Chan-Park and X. W. D. Lou, *Energy Environ. Sci.*, 2012, 5, 9453-9456.
55. Y. G. Wang, H. Q. Li and Y. Y. Xia, *Adv. Mater.*, 2006, 18, 2619-2623.
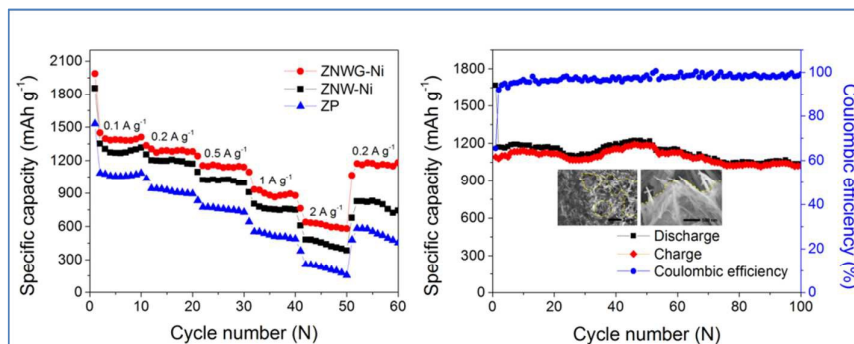
We have successfully prepared ZNWG-Ni electrode for LIBs showing superior performance of high specific capacity, fine rate capability and remarkable cycling stability.